



# Quantitative Confocal Microscopy for Grouping of Dose–Response Data: Deciphering Calcium Sequestration and Subsequent Cell Death in the Presence of Excess Norepinephrine

Kuruba Manohar<sup>1\*</sup>, Suman Gare<sup>2\*</sup>, Soumita Chel<sup>2</sup>, Vaibhav Dhyani<sup>2</sup>, and Lopamudra Giri<sup>2</sup>

## Abstract

Fluorescent calcium ( $\text{Ca}^{2+}$ ) imaging is one of the preferred methods to record cellular activity during in vitro preclinical studies, high-content drug screening, and toxicity analysis. Visualization and analysis for dose–response data obtained using high-resolution imaging remain challenging, due to the inherent heterogeneity present in the  $\text{Ca}^{2+}$  spiking. To address this challenge, we propose measurement of cytosolic  $\text{Ca}^{2+}$  ions using spinning-disk confocal microscopy and machine learning–based analytics that is scalable. First, we implemented uniform manifold approximation and projection (UMAP) for visualizing the multivariate time-series dataset in the two-dimensional (2D) plane using Python. The dataset was obtained through live imaging experiments with norepinephrine-induced  $\text{Ca}^{2+}$  oscillation in HeLa cells for a large range of doses. Second, we demonstrate that the proposed framework can be used to depict the grouping of the spiking pattern for lower and higher drug doses. To the best of our knowledge, this is the first attempt at UMAP visualization of the time-series dose response and identification of the  $\text{Ca}^{2+}$  signature during lytic death. Such quantitative microscopy can be used as a component of a high-throughput data analysis workflow for toxicity analysis.

## Keywords

calcium imaging, cell lysis, confocal microscopy, GPCR-targeting drug, fuzzy c-means clustering

## Introduction

Cytosolic calcium ( $\text{Ca}^{2+}$ ) imaging is known to be crucial for estimating drug toxicity during drug evaluation and screening, since  $\text{Ca}^{2+}$  signaling plays important roles in regulation of cell physiology, apoptosis, and necrosis.<sup>1,2</sup> Recently, many scientists focused on investigating different imaging modalities and data analysis techniques to improve the estimation of cytosolic  $\text{Ca}^{2+}$  levels. For example, two-photon microscopy has been implemented to image dendritic  $\text{Ca}^{2+}$ ,<sup>3</sup> whereas light-field microscopy has been used to estimate intracellular  $\text{Ca}^{2+}$  through high-speed volumetric imaging of single neurons in *Caenorhabditis elegans*.<sup>4</sup> Moreover, various imaging methods such as FLIM (fluorescence lifetime image-scanning microscopy) have been explored for accurate estimation of  $\text{Ca}^{2+}$  in the range of 20–200 nM and for the establishment of calibration curves.<sup>5</sup> Monitoring of  $\text{Ca}^{2+}$  sequestration at the subcellular level remains challenging, however, since it requires the collection of fluorescent signals from various planes during

volumetric imaging using advanced microscopy.<sup>6</sup> Currently, most existing systems, including plate readers and fluorescent microscopes, are not capable of providing the information present inside the cell, which requires elimination of out-of-focus light through the pinhole placed before the detector.<sup>7</sup>

<sup>1</sup>Department of BioTechnology, Indian Institute of Technology Hyderabad, Sangareddy, India

<sup>2</sup>Department of Chemical Engineering, Indian Institute of Technology Hyderabad, Sangareddy, India

\*These authors contributed equally to this work.

Received Jan 15, 2021, and in revised form Apr 14, 2021. Accepted for publication May 3, 2021.

Supplemental material is available online with this article.

### Corresponding Author:

Lopamudra Giri, Department of Chemical Engineering, Indian Institute of Technology Hyderabad, Kandi, Sangareddy, Telangana 502285, India.  
Email: giril@che.iith.ac.in

Traditional imaging methods for high-content screening,<sup>8,9</sup> based on fluorescent microscopes, have an inherent disadvantage due to the large amount of out-of-focus light coming from other focal planes.<sup>7</sup> Also, traditional fluorescent microscopy suffers from other disadvantages, including photobleaching. In contrast, confocal imaging provides imaging of a single focal plane and control over choosing field depth.<sup>10–12</sup> Recently, there has been significant improvement in the direction of high-content imaging in real-time monitoring of signaling dynamics in single cells.<sup>13,14</sup> Although laser scanning confocal microscopy is one of the approaches that can be used for measuring subcellular  $\text{Ca}^{2+}$  dynamics, the imaging speed is compromised.<sup>15</sup> Hence, we choose to use spinning-disk microscopy to perform cytosolic- $\text{Ca}^{2+}$  imaging in a single plane. The rationale behind using Fluo-4 as the indicator is that it is having higher dissociation rate and lower value of Kd (345 nM). Additionally, Fluo-4 has high dynamic range, brightness, and high signal-to-noise ratio among various  $\text{Ca}^{2+}$  dyes.<sup>16</sup>

It is known that 34% of drugs on the market are based on G protein-coupled receptor (GPCR)-targeting drugs<sup>17,18</sup> that are used to treat chronic heart disease, neurodegeneration, and cancer. It has also been shown that  $\text{Ca}^{2+}$  imaging can be used for drug screening and to identify the operating range of GPCR-targeting drug doses.<sup>19</sup> GPCR-targeting drugs, including norepinephrine, tizanidine, clonidine, and dexmedetomidine (examples of neuroprotective drugs), are generally used for the treatment of various neurodegenerative diseases as well as heart dysfunctions.<sup>18,20,21</sup> The evaluation of drug efficiency and ranking of drugs have been performed through *k*-means clustering of the features extracted from the  $\text{Ca}^{2+}$  response.<sup>19</sup>

An increased level of norepinephrine is known to stimulate cardiac autophagy and hypertrophy.<sup>22</sup> In fact, excess norepinephrine is known to cause oxidative stress and cell death. Existing studies mostly concentrate on the mechanisms corresponding to lower levels of norepinephrine.<sup>23</sup> Despite knowing the adverse effects of norepinephrine, the responses in the presence of higher levels of norepinephrine are not explored. Specifically, large-scale studies and identification of  $\text{Ca}^{2+}$  signatures for a longer duration have not been performed. In this context, we propose imaging using confocal imaging and visualization of a dataset of a large number of videos on  $\text{Ca}^{2+}$  dynamics using uniform manifold approximation and projection (UMAP). To the best of our knowledge, this is the first instance of studying cell death dynamics through confocal imaging of cytosolic  $\text{Ca}^{2+}$  and identification of various  $\text{Ca}^{2+}$  signatures using fuzzy clustering. In addition, we present a detailed comparison of  $\text{Ca}^{2+}$  dynamics at low and high levels of norepinephrine.

In this article, we choose norepinephrine that targets  $\alpha_2$  adrenergic receptors ( $\alpha_2\text{ARs}$ ), since the underlying mechanism for inducing toxicity is crucial in determining the drug dose range for modulating cardiac function.<sup>24–26</sup> Clinical

trials have shown that norepinephrine can be used for the treatment of hypotension and maintaining mean arterial pressure in the intensive care unit (ICU) setting as well as during caesarian delivery. It has been found that norepinephrine has been tested in such clinical trials with perfusion of approximately 0.05–2  $\mu\text{g}/\text{Kg}\cdot\text{min}$  of norepinephrine using an intravenous pump.<sup>22</sup> In several other cases, however, it has been reported that higher drug doses may be lethal by activating apoptosis by creating  $\text{Ca}^{2+}$  overload in the mitochondrial matrix.<sup>23</sup> Hence, a toxicity study assumes importance for determining the safe ranges of drug doses and  $\text{Ca}^{2+}$  levels under higher levels of norepinephrine.

Previous studies mostly concentrate on toxicity studies based on protein expression and quantification of viability and the percentage of apoptotic cells using annexin V.<sup>21</sup> Recent work shows that flow cytometry has been implemented to measure cytosolic and mitochondrial  $\text{Ca}^{2+}$  to monitor apoptosis.<sup>21</sup> These techniques, however, are able to capture only the  $\text{Ca}^{2+}$  level at a lower resolution. Moreover, fluorescent and confocal microscopy also have been used for studying the apoptotic process through the measurement of intracellular  $\text{Ca}^{2+}$ .<sup>27</sup> However, obtaining the correlation between cellular responses and death dynamics remains challenging due to the unavailability of tools that can be used for quantitative imaging. In this article, we demonstrate a methodology for high-resolution imaging that provides the  $\text{Ca}^{2+}$  dynamics in subcellular parts in the presence of high levels of norepinephrine.

One of the major challenges for analyzing a large number of time-lapse  $\text{Ca}^{2+}$  imaging videos is to visualize and quantify the spatiotemporal dynamics of  $\text{Ca}^{2+}$  level obtained through time-lapse imaging. In this context, the development of tools in combination with high-content imaging and automated analysis is expected to increase the quality of molecules progressing to preclinical stages during the drug development pipeline.<sup>28</sup> Previously, various clustering techniques including *k*-means and hierarchical clustering, based on Euclidian and correlation distances, have been used to group the cells with respect to a  $\text{Ca}^{2+}$ -spiking patterns shown by them in a population.<sup>29–31</sup> There is, however, less investigation in clustering analysis that divides the  $\text{Ca}^{2+}$  time-series data points into groups, such that distributions of patterns corresponding to lower and higher drug doses are deciphered.

Recently, a nonlinear dimensionality reduction technique, UMAP, has been developed for the analysis of high-dimensional data.<sup>32</sup> In the current work, we propose a computational framework based on UMAP and fuzzy *c*-means (FCM) clustering, which generates a complete visualization of a dataset for  $\text{Ca}^{2+}$  dynamics and finds the relative distribution of various responses in a dose range. The rationale behind choosing FCM is to perform a probabilistic allocation for the points that can be a part of various clusters.

In this article, we propose an integrated framework for the measurement and analysis of  $\text{Ca}^{2+}$  in single cells through live cell imaging using spinning-disk confocal microscopy. First, we provide a detailed protocol for imaging using confocal microscopy. Second, this work highlights the use of UMAP for visualization and interpretation of spiking responses at various doses. The toolbox based on UMAP and FCM is efficient and fast, such that standard desktop computers can process the data in a few seconds. The specific novelty of the proposed study is to demonstrate the feasibility of using UMAP and FCM to identify distinctly different responses. Furthermore, reclustering of high dose responses shows that there are three distinct responses, among which one corresponds to the accumulation of  $\text{Ca}^{2+}$  in subcellular parts followed by cell blebbing and lytic death. The quantitative imaging reveals the specific signature of  $\text{Ca}^{2+}$  dynamics that lead to cell death.

## Materials and Methods

### Cell Culture

HeLa cells were cultured in Dulbecco's modified Eagle medium (DMEM; Cellgro, Manassas, VA) supplemented with 10% dialyzed fetal bovine serum (Atlanta Biologicals, Flowery Branch, GA). The cells were grown in 29 mm glass-bottom dishes (In Vitro Scientific, Sunnyvale, CA) and were maintained in culture until 70–80% confluency.

### Imaging Setup Using Spinning-Disk Confocal Microscopy

Cells seeded on 29 mm glass-bottom dishes were imaged (48 h after seeding the cells) using a Leica spinning-disk confocal-imaging system (Leica Microsystems, Wetzlar, Germany) that has an Andor FRAPPA device and electron-multiplying charge-coupled device (EM-CCD) camera (Andor, Belfast, UK). During the entire duration of  $\text{Ca}^{2+}$  imaging, HeLa cells were maintained in Hank's Balanced Salt Solution (HBSS; Invitrogen, Life Technologies, Grand Island, NY) at 37°C, 5%  $\text{CO}_2$ , in an incubator that is attached to the microscope. To avoid the decrease in fluorescent intensity through drifts in the imaging plane, an adaptive focus control (AFC) was used. Specifically, a 63× oil objective was used to find the  $\text{Ca}^{2+}$  spiking in subcellular parts. Fluorescent images were acquired with argon laser, excited at 488 nm for tracking Fluo-4 (Molecular Probes, Life Technologies, Grand Island, NY) intensity.

### Fluorescent Dye Labeling and $\text{Ca}^{2+}$ Imaging for Monitoring Cell Death

$\text{Ca}^{2+}$  imaging was performed in HBSS. Cell cultures were loaded with 2  $\mu\text{M}$  Fluo-4 for 30 min in HBSS at 25°C.

Then, the cells were washed with HBSS three times with a 10 min incubation time for each of the washes. Time-lapse imaging was performed before and after adding the drug. The Fluo-4 images (excitation: 488 nm; emission: 510 nm) were acquired at approximately 3–4 s intervals at 37°C. Norepinephrine (Sigma-Aldrich, St. Louis, MO) in HBSS was used to activate the  $\alpha_2\text{AR}$  at various doses. To cover a wide range of agonist concentrations, the cells were treated with nine different concentrations (0.1  $\mu\text{M}$ , 0.5  $\mu\text{M}$ , 1  $\mu\text{M}$ , 10  $\mu\text{M}$ , 40  $\mu\text{M}$ , 50  $\mu\text{M}$ , 100  $\mu\text{M}$ , 200  $\mu\text{M}$ , and 400  $\mu\text{M}$ ) of norepinephrine. Time-lapse imaging was used to construct the videos to monitor the cell fate dynamics and  $\text{Ca}^{2+}$  level for 615 s.

### Differential Interference Contrast Imaging and a Propidium Iodide Hoechst Assay for Cell Lysis

HeLa cells were washed three times with HBSS (Gibco, Grand Island, NY) before differential interference contrast (DIC) imaging using a laser scanning confocal microscope (SP8 Lightning, Leica Microsystems). To detect the cell lysis, cells were stained with 2.5  $\mu\text{g}/\text{ml}$  propidium iodide (PI; Sigma-Aldrich) and were visualized using an excitation at 561 nm and emission at 600–660 nm using a Hybrid Detector 4 (Hyd4; Leica Microsystems) and 63× oil objective in confocal microscopy.<sup>33</sup> Nuclear morphology was analyzed using Hoechst 33342 nuclear staining, and imaging was performed with a 63× oil objective (Sigma-Aldrich) at 405 nm excitation.<sup>34,35</sup> DNA condensation was visualized using a photomultiplier tube (PMT) 3 detector (emission: 420–480 nm).

### Image Analysis Measurements and Quantification

Time-lapse movies were acquired every 3–4 s for 103 s (30 frames) before agonist addition and 615 s after agonist addition. Andor IQ software was used to obtain the time course of fluorescence intensity of Fluo-4 in each cell treated with drug. For single-cell analysis, the regions of interest (ROIs) were selected around the cell periphery, and the mean fluorescent signal was collected within the ROIs (**Suppl. Fig. S1A** and **Fig. S1B**). To reduce the background noise, the intensity of each cell was calculated by subtracting the mean background intensity from the original mean intensity of each cell. Furthermore, we performed normalization as shown in **Supplementary Figure S1C** and **Fig. S1D**. For each cell in the population (each time-lapse video contains approximately 15–22 cells), the number of  $\text{Ca}^{2+}$  spikes (N) and the duration of  $\text{Ca}^{2+}$  spiking (T) were quantified using the findpeaks function in MATLAB (MathWorks, Natick, MA).

Since the dataset was obtained through acquisition of multiple videos for a large range of doses, it was found that some of the videos contain photobleaching (**Suppl. Fig. S2A**).

To correct the baseline for the photobleaching effect, we used moving-average method<sup>36</sup> using MATLAB, as shown in **Supplementary Figure S2B** and **Fig. S2C**.

### Dataset Description

The distribution of various doses in the dataset used is represented in **Supplementary Figure S3A**. First, we performed the analysis using the total dataset (Fluo-4 intensity for 395 time points for 298 cells). Then, we performed reclustering of the dataset corresponding to a higher dose, comprising a total of 395 time points corresponding to 200  $\mu\text{M}$  (39 cells) and 400  $\mu\text{M}$  (26 cells) of norepinephrine.

### Data Preprocessing

To perform correction to address the photobleaching events, first de-trending of the fluorescent traces was performed using an algorithm presented in Venkateswarlu et al.<sup>36</sup> Next, the time course of  $\text{Ca}^{2+}$  was denoised using the method of exponential moving average. The `tsmovavg` function in MATLAB was used to smoothen data. Since the Fluo-4 intensity measures are at different time points for different videos, finally Fluo-4 intensities for all videos at a fixed set of time points (395) were calculated through interpolation using the `interp1` function in MATLAB.

### Normalization

After preprocessing, we performed normalization of the dataset using  $L2_{norm}$ , which is defined on Euclidean distance:

$$L2_{norm} = \frac{A_{ij}}{\text{sqrt}\left[\sum_{j=1}^m \sum_{i=1}^n A_{ij}^2\right]}, \text{ where } A_{ij} \text{ is the}$$

data point corresponding to the  $\text{Ca}^{2+}$  level for the  $j^{\text{th}}$  cell at  $i^{\text{th}}$  time;  $n$  is the number of time points; and  $m$  is the number of cells. We have used the Python3.7 Numpy Library (Version 1.16.2) for finding the  $L2_{norm}$ .

### Running the Dimensionality Reduction Algorithm

We used the `umap-learn` library (Version 0.3.9) of Python 3.7, which computes the reduced matrix using UMAP projection.<sup>32,37,38</sup> This algorithm was run on a total dataset (395 time points  $\times$  298 cells) and a higher-doses dataset (395 time points  $\times$  65 cells). The UMAP runtime was found to be 1.07 s. We also had performed t-distributed stochastic neighbor embedding (t-SNE) for visualizing the two-dimensional (2D) projection with a runtime of 2.79 s.

### Visualization of Cell Populations and Fuzzy Clustering

To visualize the ability of the dimensionality reduction method to preserve the cohesiveness of data, we first

incorporated the categorical labels of various drug doses. To choose a putative cluster number, first we performed clustermap visualization based on hierarchical clustering using the Python Seaborn Library (Version 0.9). Since the clustermap analysis indicated that the dataset may be divided into approximately 10 distinct groups (**Suppl. Fig. S3B**), fuzzy  $c$ -means was performed on the UMAP-reduced data with  $k=10$ . Clustering analysis was performed with the fuzzy- $c$ -means library (Version 0.0.6). Moreover, for comparison with existing methods, we performed principal component analysis (PCA) and feature extraction (amplitude and number of peaks) followed by  $k$ -means and hierarchical clustering using MATLAB.<sup>19,31</sup> The comparison of various clustering methods was performed using seven different validation techniques as presented in Liang et al.<sup>39</sup>

### Comparison of $\text{Ca}^{2+}$ Spiking within a Group

We further present the similarity between the spiking profiles of all cells within and among clusters using the empirical cumulative distribution function (eCDF in MATLAB). The eCDF is a step function that jumps up by  $1/n$  at each of the  $n$  data points, thus converging to probability 1. Here, the distance between two cells was measured by calculation of pairwise root mean square error (RMSE) between the eCDFs of those two cells. The lower RMSE between the eCDFs of two  $\text{Ca}^{2+}$ -spiking profiles indicates higher statistical similarity between them. In addition, we calculated Pearson's correlation coefficient between each pair within 10 clusters.

A schematic diagram for the overall workflow proposed for visualization and analysis is presented in **Figure 1**. Also, the parameters and distances used in the algorithms are listed in **Supplementary Table S1**.

**Statistical Analysis.** One-way analysis of variance (ANOVA) was used for multiple comparisons between doses to see the difference with respect to the amplitude and number of spikes in  $\text{Ca}^{2+}$  oscillation using MATLAB.

## Results

### Time-Lapse Imaging and Single-Cell Responses

We have used a time-lapse imaging approach to obtain  $\text{Ca}^{2+}$  responses after treatment with an agonist for various doses and obtained quantitative information about collective  $\text{Ca}^{2+}$  dynamics in a group of cells cultured on a petri dish. **Figure 2** shows the heat map representation of time-lapse images obtained for two representative cell populations treated with 10  $\mu\text{M}$  and 400  $\mu\text{M}$  norepinephrine. The results show that for lower doses, the  $\text{Ca}^{2+}$  level comes back to the basal level after 3 s, whereas for higher doses, an increased level of  $\text{Ca}^{2+}$  is maintained for a longer period. To obtain a mapping of dose response from 0.1  $\mu\text{M}$  to 400  $\mu\text{M}$ , we plotted the time course of Fluo-4 intensity in multiple cells for each

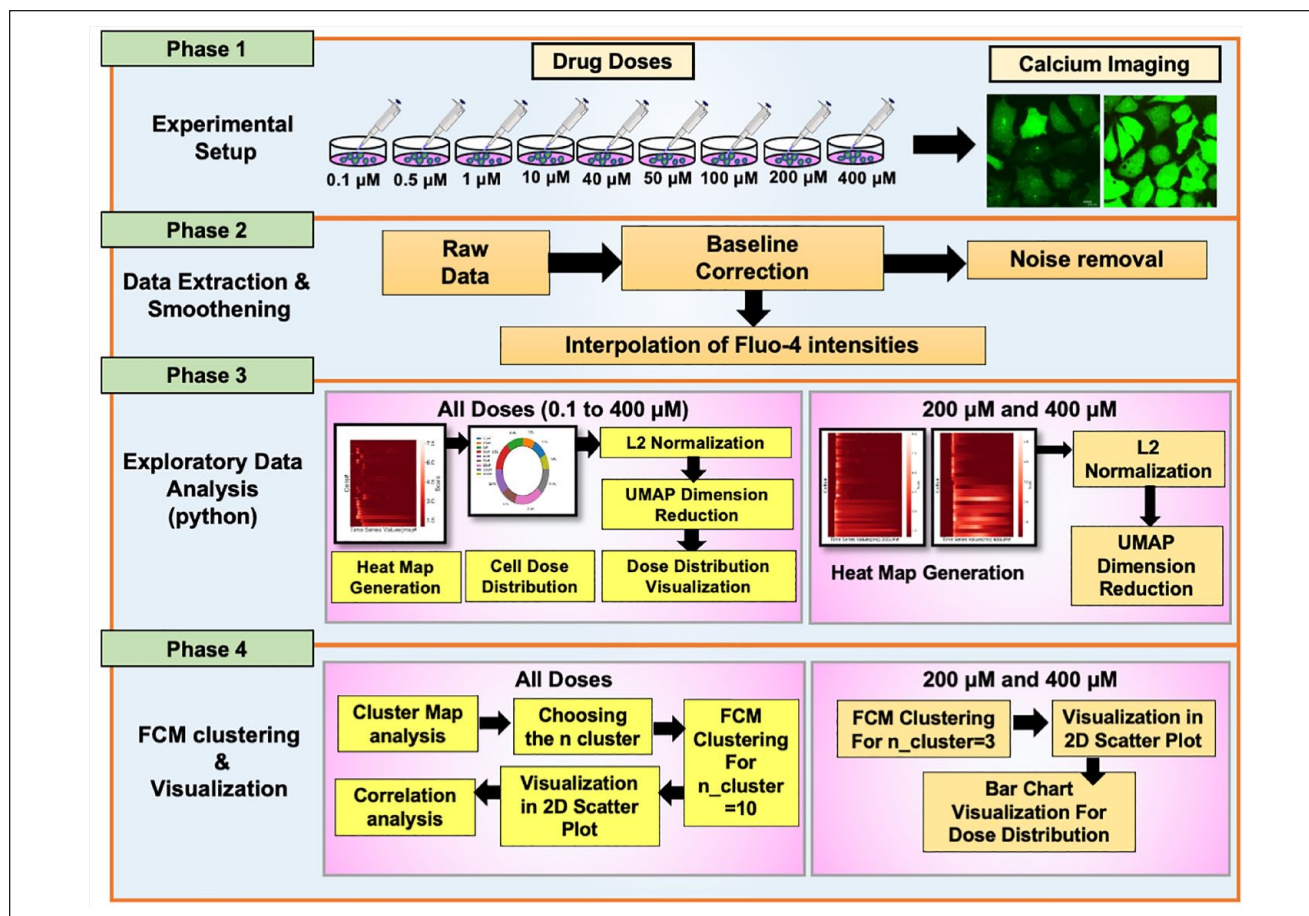


**Figure 1.** Schematic diagram for data acquisition to obtain a dose–response profile using high-resolution  $\text{Ca}^{2+}$  imaging, data visualization, and clustering of  $\text{Ca}^{2+}$  dynamics. The process is divided into four steps: (1) Live cell imaging and video acquisition for nine different doses. (2) Construction of a dose–response dataset and preprocessing. (3) Heat map representation and uniform manifold and projection (UMAP) of the entire dose–response dataset. (4) Clustering of the UMAP-projected dataset for the entire dose response using fuzzy  $c$ -means (FCM) and reclustering of high dose responses using FCM.

dose (Fig. 3). Figure 3A and 3B, 3C and 3D, 3E and 3F, 3G and 3H, and 3I and 3J present the  $\text{Ca}^{2+}$  oscillations in individual cells with drug doses of 1 μM, 10 μM, 100 μM, 200 μM, and 400 μM, respectively. When the drug dose was maintained at 0.1 or 1 μM, the cells showed a lower number of  $\text{Ca}^{2+}$  spikes and rapid damping (Fig. S4A and S4B, Fig. 3A and B). In contrast, when the drug dose was maintained at 10 μM, a higher number of  $\text{Ca}^{2+}$  spikes and higher amplitude were observed (Fig. 3C and Fig. 3D). At 100 μM, the  $\text{Ca}^{2+}$  release takes place in a periodic manner leading to sustained oscillatory responses (Fig. 3F). Figure 3G shows that the treatment of a higher dose of norepinephrine leads to elevated release of  $\text{Ca}^{2+}$  into cytosol after 9 s of drug addition, followed by rapid depletion of  $\text{Ca}^{2+}$  in 30 s. Supplementary Figure S4 shows representative responses for 0.1 μM, 0.5 μM, 40 μM, and 50 μM. The results show that the frequency of  $\text{Ca}^{2+}$  oscillation increases in some of the cells with an increase in drug dose in the range from 1 to 100 μM (Fig. 3). Supplementary Videos S1 and S2 show

the recording of Fluo-4 intensity corresponding to treatment with 10 and 100 μM norepinephrine.

### Time Course of Cytosolic $\text{Ca}^{2+}$ for a Wide Range of Drug Doses

First, we show the complete time-series dataset on responses obtained for 0.1 to 400 μM for 298 cells through the heat map representation, where the y-axis is Fluo-4 intensity for all the cells treated with various doses (Fig. 4A), and the x-axis represents time. To show a comparison between various features, including the amplitude and number of peaks of the  $\text{Ca}^{2+}$  response between nine doses, we also show the box plot analysis of amplitude and number of  $\text{Ca}^{2+}$  peaks (Fig. 4B and 4C). The results show that the range of features among doses does not yield any specific trend.

Next, we performed one-way ANOVA for pairwise comparisons between doses to investigate the dose-to-dose differences in numbers of peaks and amplitude of the  $\text{Ca}^{2+}$

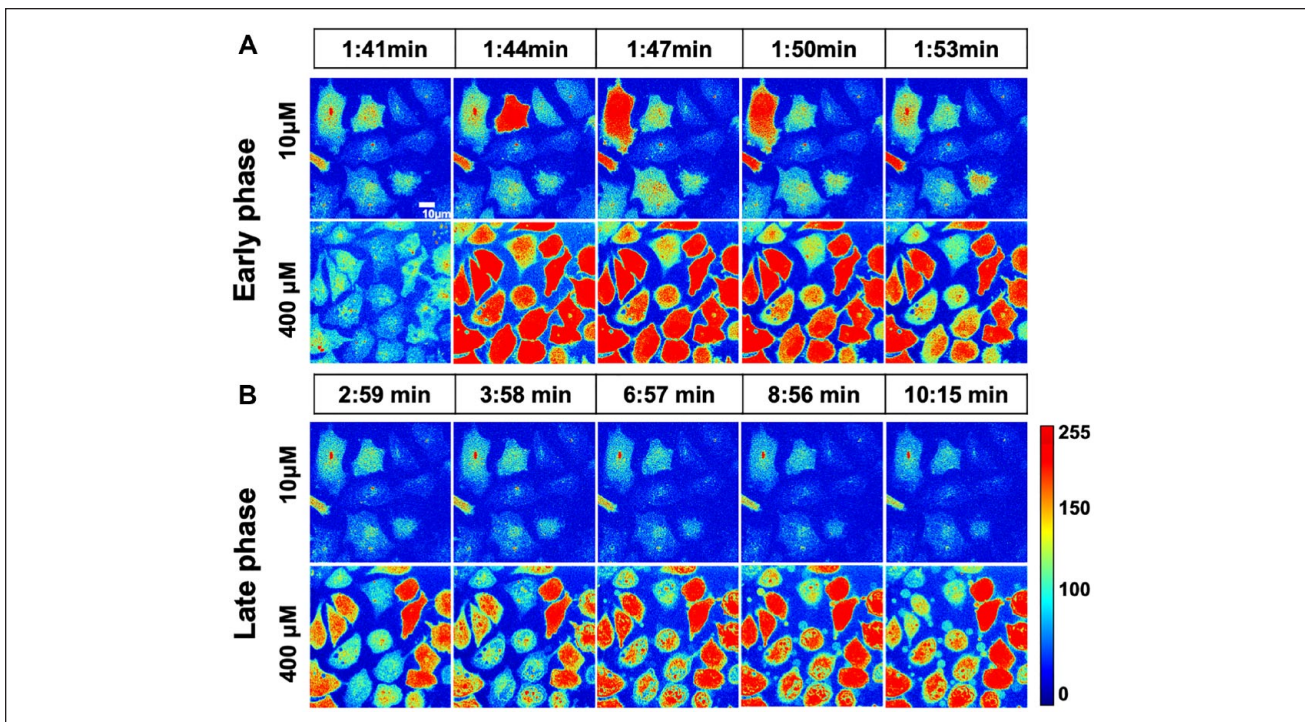


**Figure 2.** Spatial intensity mapping of Fluo-4 showing the distribution of  $Ca^{2+}$  response in a HeLa cell population ( $n = x$ ) in the presence of norepinephrine (an  $\alpha 2$ -adrenergic receptor agonist). Representative time-lapse images were collected from the videos captured using a  $63\times$  oil objective in spinning-disk confocal microscopy for 615 s. **(A)** Concentration of norepinephrine dose:  $10 \mu M$ ; **(B)** concentration of norepinephrine dose:  $400 \mu M$ . Please see figure online for color.

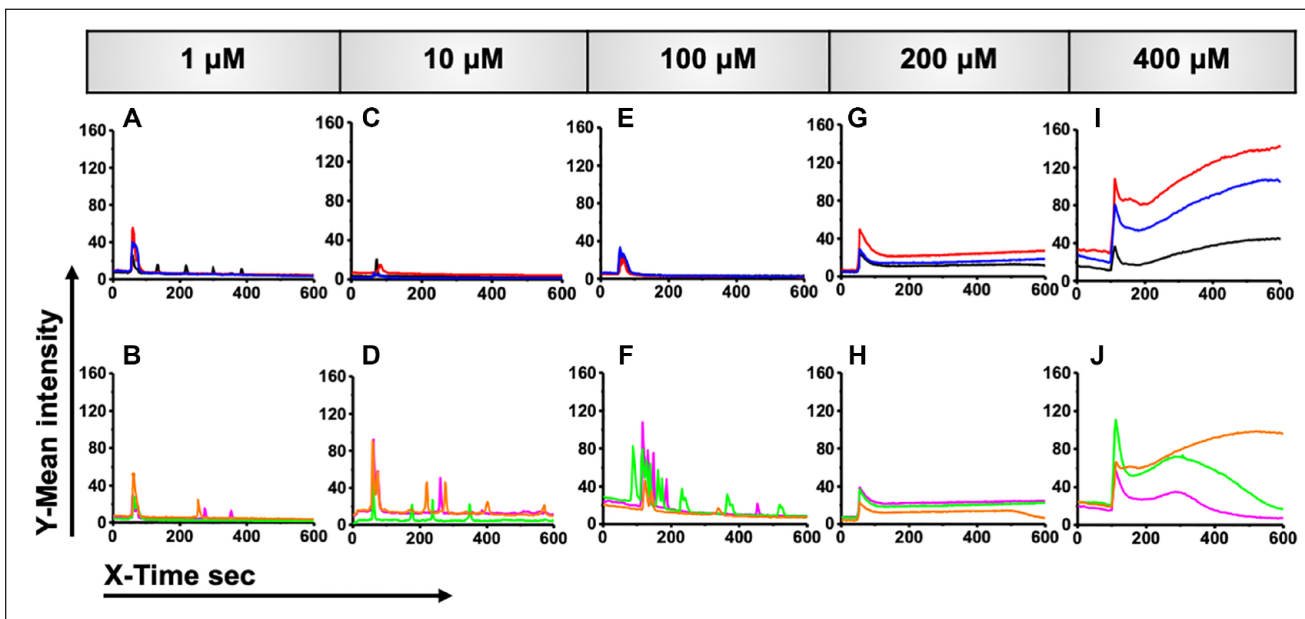


**Figure 3.** Time course of Fluo-4 intensity obtained from single cells treated with a norepinephrine dose ranging from  $1 \mu M$  to  $400 \mu M$  shows cell-to-cell variability in  $Ca^{2+}$  response. For each dose of norepinephrine, five representative fluorescent traces from individual cells are shown: **(A,B)**  $1 \mu M$ , **(C,D)**  $10 \mu M$ , **(E,F)**  $100 \mu M$ , **(G,H)**  $200 \mu M$ , and **(I,J)**  $400 \mu M$ . Y axis represents mean Fluo-4 intensity in each cell. Please see figure online for color.

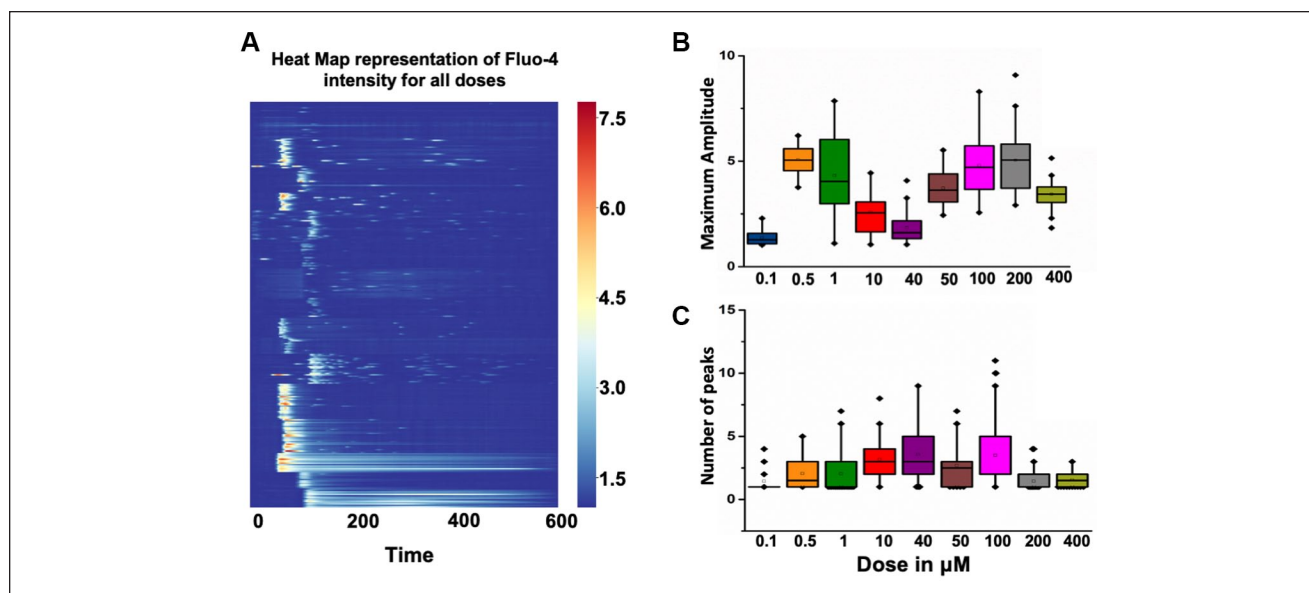


**Figure 4.** Visualization of a dose–response profile obtained from  $\text{Ca}^{2+}$ -imaging experiments. **(A)** Heat map representation of time-series events color-coded by the intensity of Fluo-4. **(B)** Box plot analysis of maximum amplitude of  $\text{Ca}^{2+}$  responses corresponding to various norepinephrine doses ranging from 0.1 to 400  $\mu\text{M}$ . **(C)** Box plot analysis of number of spikes corresponding to various norepinephrine doses ranging from 0.1 to 400  $\mu\text{M}$ . Please see figure online for color.

responses. **Supplementary Figure S5** provides the pairwise heatmap of  $p_{ij}$ -values obtained from ANOVA analysis, in which  $p_{ij}$  denotes the  $p$ -value (with  $\alpha = 0.05$ ) corresponding to the comparison of the  $i^{\text{th}}$  dose with the  $j^{\text{th}}$  dose, [ $i = 1, 2, \dots, 9; j = 1, 2, \dots, 9$ ], with respect to number of peaks and amplitude. The results clearly show that for most of the cases, the maximum amplitude is significantly different when compared between two doses. For a few cases, however, there is no significant difference in the amplitude of  $\text{Ca}^{2+}$  response between low and high doses (**Suppl. Fig. S5A**). In contrast, for a larger number of cases, there is no significant difference between the number of peaks for higher doses compared to lower doses (**Suppl. Fig. S5B**). Overall, the analysis indicates that due to the huge variability present under the same dose, there might not be any statistical significance between some doses. This may arise, however, due to the fact that time information is lost when the feature depends on only the number of  $\text{Ca}^{2+}$  spikes. Although one-way ANOVA indicates that there is significant difference between the multiple doses, such a conventional approach does not provide the overall pattern present in the data. To address this, we present a schematic diagram of the workflow that describes various steps of the dose–response analysis (**Fig. 1**).

### UMAP Visualization and Fuzzy C-Means Clustering

Since single-cell  $\text{Ca}^{2+}$  dynamics for various doses give rise to high-dimensional data, we have implemented UMAP to convert the information to a lower dimension. UMAP is

known to be very efficient at embedding large high-dimensional datasets. **Supplementary Figure S6** shows the comparison of 2D embedded data obtained from PCA and UMAP. The result clearly shows that UMAP performs better at separating the data points compared to PCA. We ran UMAP on the dataset covering nine doses on HeLa cells (**Fig. 5A** and **Suppl. Fig. S6**). The UMAP visualization clearly shows that each of the cell responses is assigned to a specific point in a 2D plot. Moreover, each dose can be visualized as a combination of cells in 2D plots (**Fig. 5A**). Next, by color coding the actual doses in UMAP representation, we observed that the cells treated with similar doses remain in the close neighborhood in 2D plots (**Fig. 5A**).

After UMAP reduction, we found that many data points could go to more than one cluster. Hence, we performed fuzzy  $c$ -means clustering for grouping the time-series events into 10 broad types (**Fig. 5B** and **Suppl. Fig. S7**). Moreover, UMAP and FCM were found to be reasonable in pulling together clusters corresponding to similar responses with distinct amplitude ranges (**Suppl. Fig. S7**). The result clearly shows that FCM is able to identify clusters 1, 2, 5, 6, 7, 8, and 9, in which each cluster represents a similar spiking pattern (**Fig. S7**).

**Supplementary Figure S9A** shows the box plot representation of the correlation coefficient between two cells present in the same cluster. In addition, we show a heatmap representation of the pairwise RMSE between the cumulative density functions (CDFs) obtained from a single-cell  $\text{Ca}^{2+}$ -spiking profile (**Suppl. Fig. S9B**). The results clearly show that RMSE values between the CDFs of the cells within the clusters (along the leading diagonal) are less

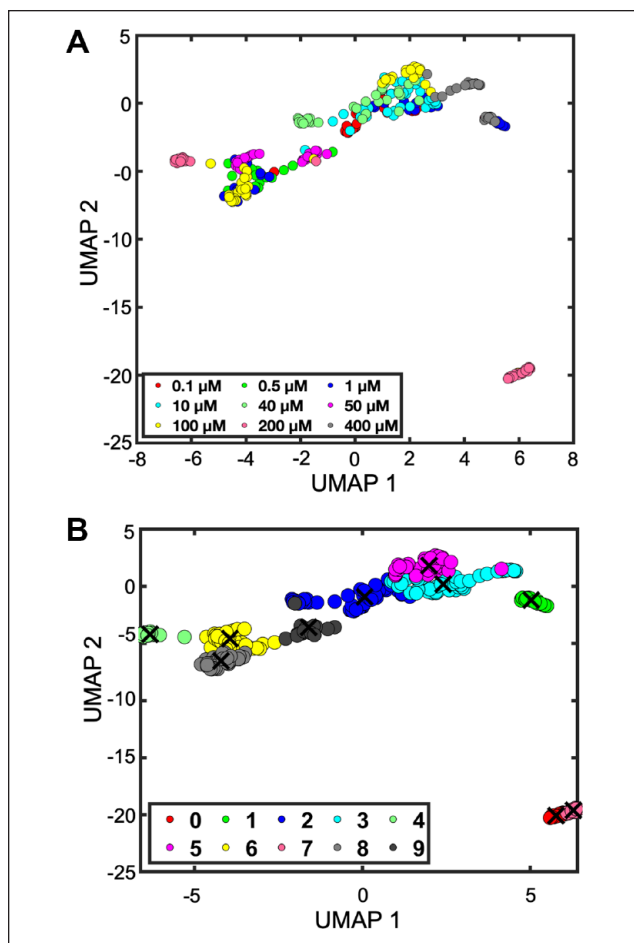


**Figure 5.** Uniform manifold and projection (UMAP) embed the overall structure of dose–response data based on measurement of  $\text{Ca}^{2+}$ . (a) UMAP of fluorescent traces color-coded according to the norepinephrine dose. (b) UMAP and fuzzy  $c$ -means clustering of  $\text{Ca}^{2+}$  responses ( $k = 10$ ). Please see figure online for color.

compared to RMSE values between the CDFs of cells across clusters. This indicates that UMAP and FCM were able to divide the  $\text{Ca}^{2+}$  spiking into groups in which responses are statistically similar.

While UMAP is able to segregate the data into distinct island regions corresponding to one cluster, back mapping of time-series data shows that clusters 0 and 4 show a spiking pattern of distinct features and cluster 3 shows the noisy responses corresponding to low drug doses (Suppl. Fig. S7). Also, cluster 4 is one of the 10 clusters in which the responses are mixed and do not elicit a distinct spiking pattern (Suppl. Fig. S8A). Instead of spiking frequency, in this case, UMAP and FCM ordered the events according to their amplitude. We observed that FCM was able to identify two clusters (cluster 4 and cluster 5) that contain  $\text{Ca}^{2+}$  responses with higher amplitude and lower frequencies (Suppl. Fig. S8). Specifically, cluster 5 represents a group of time-series events in which the  $\text{Ca}^{2+}$  level is consistently maintained at

a higher level instead of having a typical oscillatory nature (Suppl. Fig. 8B). Supplementary Figure S10A shows the distribution of doses in various clusters, whereas Supplementary Figure S10B shows the distribution of responses from different clusters among various doses. Back mapping of the distribution of responses shows that each dose contains various types of responses obtained from the clustering process.

To show that the proposed quantitative confocal microscopy with UMAP visualization and FCM clustering is better than the other existing methods, we performed an analysis of the above dataset with six methods: (1) feature extraction and  $k$ -means clustering, (2) feature extraction and FCM clustering, (3) PCA and  $k$ -means clustering, (4) feature extraction and hierarchical clustering, (5) UMAP and hierarchical clustering, and (6) UMAP and fuzzy clustering. Supplementary Figure S11 shows the visualization of the data and clusters using these six methods. Next, we present a comparison of the six methods using a heatmap for pairwise Pearson correlation coefficients within clusters (Suppl. Fig. S12). In addition, a comparison of the distribution of clusters among doses is shown in Supplementary Figure S13. Finally, the methods were compared using seven clustering validation indices, which are presented in Table 1. Overall, the results show that UMAP visualization and FCM clustering provide a better way to analyze the dataset for grouping the responses.

### Single-Cell $\text{Ca}^{2+}$ Dynamics for Higher Drug Doses

Based on these results, we reclustered the  $\text{Ca}^{2+}$  dynamics in cells treated with 200 and 400  $\mu\text{M}$  of norepinephrine (Fig. 3H and 3I). Supplementary Figure S14A and S14B shows the heat map of the Fluo-4 intensity corresponding to 200  $\mu\text{M}$  and 400  $\mu\text{M}$ . Although these two doses contain cells with a higher  $\text{Ca}^{2+}$  level, they retain significant heterogeneity. Hence, we reclustered the high-dose dataset and identified three clusters (clusters A, B, and C) using FCM (Suppl. Fig. S14C). This time, UMAP and FCM were able to distinguish the time-series events according to their damping time within these three clusters. Figure 6A–6C shows the  $\text{Ca}^{2+}$  dynamics for three major clusters, in which cluster C indicates the group containing  $\text{Ca}^{2+}$  responses having two major peaks. Figure 6D shows the mapping back of the response distribution corresponding to three clusters. The results show that the time-series data corresponding to higher drug doses can be grouped and visualized using a reduction of dimension using UMAP.

### Spatial Mapping of Cytosolic $\text{Ca}^{2+}$ in Single Cells

To identify the specific pattern of  $\text{Ca}^{2+}$  accumulation in cells of cluster A obtained from reclustering the dataset corresponding



**Table 1.** Comparison of Various Methods for Analysis of  $\text{Ca}^{2+}$  Response Using Seven Internal and External Clustering Validation Indices.

Method	WB	Silhouette	Calinski–Harabasz	Davies–Bouldin	Dunn	S_Dbw	AI
A	1.115	0.512	287.061	0.806	0.013	0.141	0.091
B	0.609	0.689	525.317	0.642	0.023	0.139	230.531
C	1.038	0.521	308.153	0.816	0.005	0.145	0.104
D	0.187	0.648	1710.359	0.673	0.030	0.012	260.450
E	171.307	-0.698	1.868	13.378	0.001	0.154	0.363
F	17.695	-0.017	18.085	1.096	0.000	0.172	0.016

(A) *k*-means clustering of feature-based data. (B) PCA followed by *k*-means. (C) FCM clustering of feature-based data. (D) UMAP followed by FCM. (E) UMAP followed by hierarchical clustering. (F) Hierarchical clustering of feature-based data (green: rank 1; and yellow: rank 2). The two features used were the maximum amplitude of  $\text{Ca}^{2+}$  response and the number of peaks in a given duration. AI, Artificial intelligence; FCM, fuzzy *c*-means; PCA, principal component analysis; UMAP, uniform manifold and projection; WB, WB-index for cluster validation. Please see table online for color.

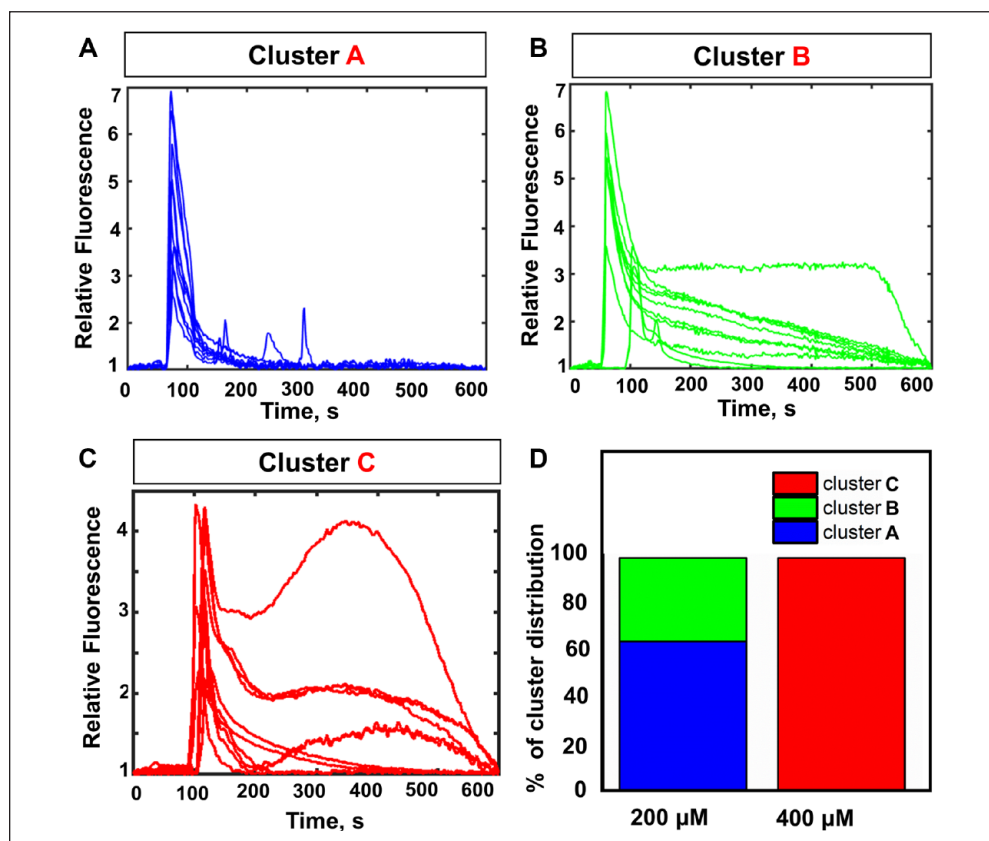


**Figure 6.** Single-cell landscaping of  $\text{Ca}^{2+}$  dynamics at higher doses. (A–C) Single-cell fluorescent traces corresponding to three clusters (A, B, and C, respectively) obtained from the high-dose dataset by fuzzy *c*-means (FCM). (D) Mapping back of the distribution of various response types corresponding to 200 and 400  $\mu\text{M}$  of norepinephrine. Please see figure online for color.

to the high dose, we further focused on spatial mapping of  $\text{Ca}^{2+}$  levels in single cells. Specifically, to have a correlation between  $\text{Ca}^{2+}$  traces and cell fate, we show the specific  $\text{Ca}^{2+}$  signature corresponding to the higher dose of norepinephrine. **Figure 7A** shows the impact of higher drug doses on cytosolic  $\text{Ca}^{2+}$  along with the cell morphology corresponding to cluster C. **Figure 7B** shows the corresponding spatial intensity mapping describing the sequestration of  $\text{Ca}^{2+}$  into small subcellular domains. Specifically, confocal

imaging of Fluo-4 intensity reveals that the released  $\text{Ca}^{2+}$  is sequestered in specific intracellular regions in the cell (180–615 s after the addition of drug). Also, we found that the sequestration of  $\text{Ca}^{2+}$  leads to the formation of extracellular projections and cell blebbing between 240 and 615 s (**Suppl. Video S3**). The time course of  $\text{Ca}^{2+}$  concentration shows a sigmoidal increase of  $\text{Ca}^{2+}$  levels in specific intracellular regions after the initial fall in  $\text{Ca}^{2+}$  levels. These results suggest that the initiation of drug-mediated lysis can

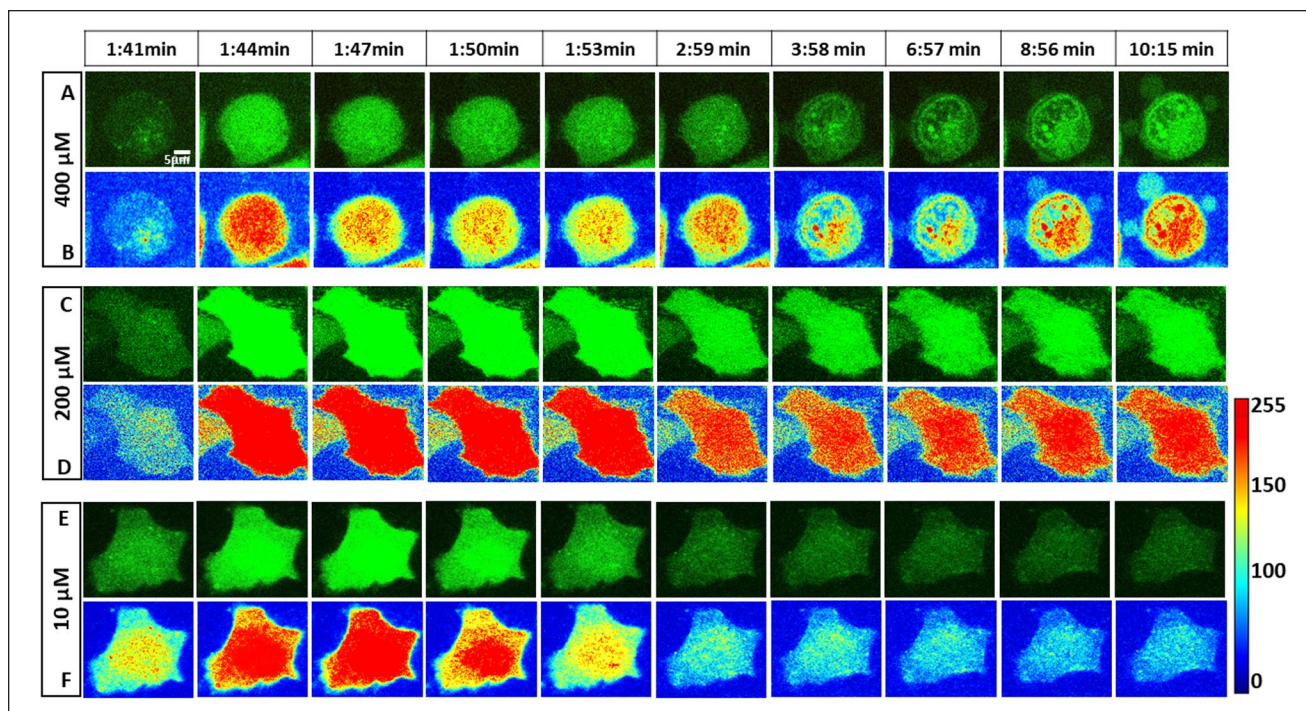


**Figure 7.** Characteristic fluorescent images and spatial heat mapping of three distinct  $\text{Ca}^{2+}$  responses. **(A,B)** Representative time-lapse images and heat maps of the distribution of cytosolic  $\text{Ca}^{2+}$  in single cells that have  $\text{Ca}^{2+}$  sequestration in microdomains and are undergoing formation of apoptotic bodies (cluster 3; dose = 400  $\mu\text{M}$ ). **(C,D)** Cells with high levels of  $\text{Ca}^{2+}$  for a longer period of time (cluster 2; dose = 200  $\mu\text{M}$ ). **(E,F)** Cells in which the  $\text{Ca}^{2+}$  level returns to the basal level after a few oscillations (cluster 1) in the presence of a low drug dose (control; dose = 10  $\mu\text{M}$ ). Please see figure online for color.

be correlated to a specific signature in a single cell (cluster C). The ability to monitor the  $\text{Ca}^{2+}$  oscillations and spatial mapping on Fluo-4 intensity allowed us to quantify  $\text{Ca}^{2+}$  dynamics during cell blebbing and cell death (**Fig 7A and B, and Suppl. Videos S3 and S4**).

In contrast, distinctly different traces are obtained for cells from cluster B (**Fig. 7C**): The spatial mapping reveals that, unlike cluster C, the  $\text{Ca}^{2+}$  level remains high for a longer period of time. Also, the  $\text{Ca}^{2+}$  level in cells treated with 200  $\mu\text{M}$  (cluster B) is not sequestered in microdomains, like it is in cells from cluster C (**Suppl. Video S5**). Next, we show a similar spatial mapping corresponding to a cell treated with 200  $\mu\text{M}$  of norepinephrine (**Fig. 7D**). **Figure 7E** shows the time-lapse images of cytosolic  $\text{Ca}^{2+}$  corresponding to the low dose (norepinephrine = 10  $\mu\text{M}$ ), and **Figure 7F** shows the spatial mapping of  $\text{Ca}^{2+}$  concentration in a single cell. Also, **Figure 7E** shows that the  $\text{Ca}^{2+}$  level goes down to the basal level of cytosolic  $\text{Ca}^{2+}$  after 107 s, and the cell retains its normal morphology (**Suppl. Video S6**).

**Supplemental Figure S15A** depicts the specific  $\text{Ca}^{2+}$  dynamics that lead to cell blebbing and lytic death. It also shows one-to-one mapping between the cell state and time course of  $\text{Ca}^{2+}$ . The schematic diagram for a possible mechanism of  $\text{Ca}^{2+}$  accumulation in the cellular microdomain corresponding to low and high doses of  $\text{Ca}^{2+}$  is shown in **Supplemental Figure S15B**. The results show that the

proposed framework is able to identify the specific features of the  $\text{Ca}^{2+}$  signature in cells in the presence of excessive norepinephrine.

To confirm cell lysis, we performed time-lapse imaging of cells treated with 400  $\mu\text{M}$  norepinephrine using a PI assay. **Supplemental Figure S16** shows a comparison of PI staining for cells with no treatment versus cells treated with 100  $\mu\text{M}$  and 400  $\mu\text{M}$ . The result clearly shows that the morphology of the cells remains unaffected without treatment with norepinephrine (**Suppl. Video S7**). In addition, no lysis was noticed for the control case. Also, the treatment with 100  $\mu\text{M}$  does not induce cell lysis within 25 min (**Suppl. Video S8**). In contrast, during treatment with 400  $\mu\text{M}$  norepinephrine, PI staining appeared at around 300 s (**Suppl. Video S9**). Since the cells were losing membrane integrity, this allowed PI to be internalized, indicating cell lysis. **Supplementary Figure S17** shows the DIC time-lapse images and spatial mapping of PI staining in single cells for the three cases described above. The results indicate that the cell morphology undergoes significant change with 400  $\mu\text{M}$  norepinephrine compared to 100  $\mu\text{M}$  or no treatment. In addition, cell blebbing was visible in the case of excess norepinephrine (**Suppl. Fig. S17A and Suppl. Video S9**).

To validate the proposed method, we further compared the method with a lysis assay using PI and a DNA-staining assay with Hoechst 33342. The results show the change in

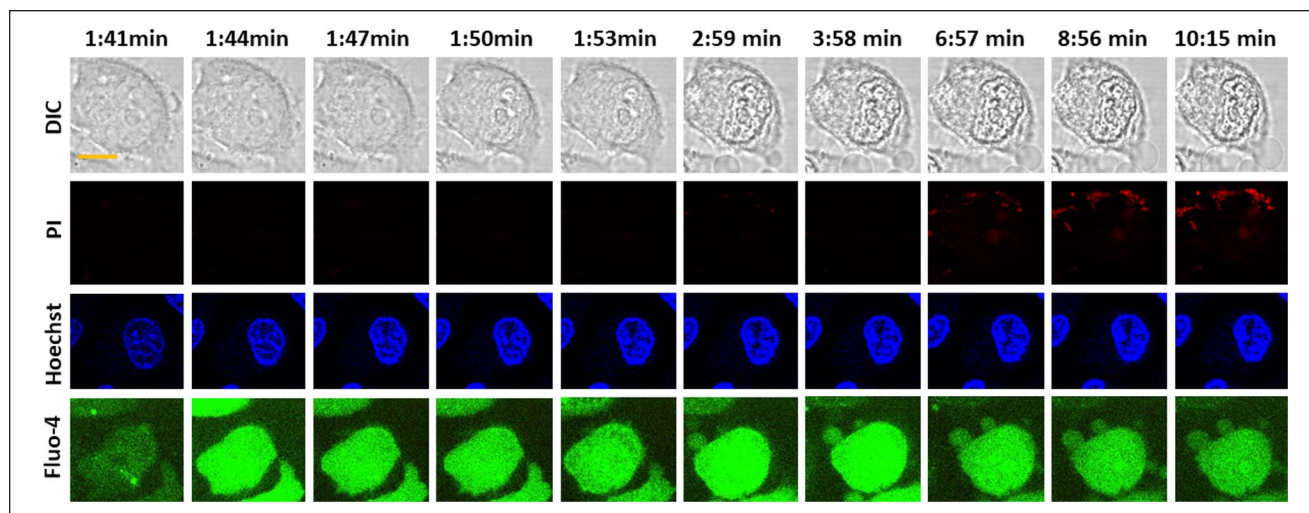


**Figure 8.** Comparison of various imaging techniques for measuring cell lysis and cell death using confocal microscopy. Comparison of signals obtained from time-lapse imaging: (**Panel 1**) Cell morphology using differential contrast imaging (DIC); (**Panel 2**) cell lysis using three-dimensional (3D) imaging of propidium iodide (PI) intensity; (**Panel 3**) nuclear morphology using two-dimensional (2D) imaging of Hoechst 33342; and (**Panel 4**) cytosolic  $\text{Ca}^{2+}$  imaging using 2D imaging of Fluo-4 in one focal plane. In each of the cases, the HeLa cell population was treated with 400  $\mu\text{M}$  norepinephrine, and images were captured using a 63 $\times$  oil objective for 10 min 15 s. Scale bar = 10  $\mu\text{m}$ . Please see figure online for color.

cell shape and the increase in Hoechst 33342 during 0–200 s. Generally, the toxicity of cells is tested using cell shape and a PI assay.<sup>33</sup> **Figure 8** shows the comparison of time-lapse imaging based on confocal microscopy of cytosolic  $\text{Ca}^{2+}$  with an established method like DIC imaging, PI, and Hoechst staining.<sup>33–35</sup> We performed DNA staining using Hoechst 33342 and time-lapse imaging, as shown in **Figure 8** (panel 3). The results show that there is an increase in the Hoechst signal with time (**Suppl. Video S10**). In addition, PI staining clearly shows that there is an onset of lysis from 3 to 7 min for cells treated with 400  $\mu\text{M}$  of norepinephrine (**Fig. 8**, panel 2). The change in signal for the Hoechst and PI assay is rather lower compared to the Fluo-4 signal (**Fig. 8**, panels 2–4). We also performed a comparison cytosolic  $\text{Ca}^{2+}$  imaging using a fluorescent microscope system and a confocal microscope (**Suppl. Fig. S18**). The result clearly shows that the signal-to-noise ratio is much better for confocal imaging compared to traditional fluorescent microscopy. Specifically, the toxicity analysis can be better performed through imaging of a confocal plane. Moreover, the increase in  $\text{Ca}^{2+}$  can be detected at 120–200 s, whereas the PI staining for lysis appears after 300 s and becomes prominent at 600–700 s (**Suppl. Fig. S17**).

## Discussion

In this work, we propose live imaging-based testing of ligands and identify specific  $\text{Ca}^{2+}$  signatures using machine learning tools. Specifically, we performed dimension reduction of the dose–response dataset

followed by clustering of  $\text{Ca}^{2+}$  responses. Particularly, we performed reclustering of responses obtained with higher drug doses. To observe the time course of events at various drug doses, we performed Fluo-4 imaging using a 63 $\times$  objective in spinning-disk confocal imaging. Also, we showed that the proposed computational framework is capable of identifying the cell death dynamics that are correlated with accumulation of  $\text{Ca}^{2+}$  in subcellular parts. This work shows a proof of concept that such an assay can be used for monitoring cell dynamics and  $\text{Ca}^{2+}$  signature during cell death.

Although higher resolution in spatiotemporal distribution of  $\text{Ca}^{2+}$  can be obtained by 3D imaging,<sup>36</sup> here we performed 2D imaging because 3D imaging leads to a reduction in time resolution and increase in imaging time. Another drawback for large-scale 3D imaging is that there is no suitable software that can be used for quantification of total fluorescent intensity within the specific volume obtained through 3D reconstruction. Moreover, more resources are needed in terms of memory and computation time for the reconstruction of z-stacks, visualization of  $\text{Ca}^{2+}$  oscillations, volumetric segmentation, and data analysis.<sup>36</sup> The current method is based on 2D imaging of cytosolic  $\text{Ca}^{2+}$  in a confocal plane, and some confocal images may appear oversaturated. Due to this, the quantitation may give a reduced value of fluorescence measurement compared to the actual value of fluorescence. Although measurement of higher concentrations of  $\text{Ca}^{2+}$  is one of the limitations of the proposed technique, the error arising from unwanted pixels was minimized using background correction, as mentioned in **Supplementary Figure S1**.

Although the expression of single reporter biomolecules can be used for live monitoring and for generating dynamic data on apoptotic processes using high-resolution microscopy,<sup>40</sup> the major disadvantage is lower transfection efficiency. This method has the ability to monitor transfected cells, which are around 30–40% of the whole cell population.<sup>41</sup> Hence, in large-scale data acquisition on multiple doses, and mapping of toxicity remains challenging using transfection-based methods.

Although differentiation between lytic and apoptotic death is outside the scope of this work, the proposed assay can be updated for simultaneous monitoring of other dyes, including caspase-8 reporter and mitochondrial (Mitotracker) dye, along with  $\text{Ca}^{2+}$ . Fluorometric characteristics have to be chosen such that there are no overlapping signals.<sup>33,40</sup> It was observed that imaging with multiple dyes, including PI–Fluo-4 and Hoechst–Fluo-4, leads to overlapping signals, different rates of internalization of the dye, and modification in toxicity levels. Hence, to quantify the toxicity or lytic process in the presence of norepinephrine, it was not possible to perform imaging using combinations of Fluo-4 and PI or Fluo-4 and Hoechst.

Recently, cell viability and cytotoxicity assays have assumed significant importance in drug screening and pre-clinical studies. Especially, dynamical feature extraction from quantitative phase imaging has been proved to be suitable for cell death detection.<sup>33</sup> Time-lapse imaging of cell morphology and cell mass topography during cell death has been used to classify cell death into two types: apoptosis and cell lysis. Since it has been reported that lytic death is associated with the formation of large cytoplasmic membrane blebs or multiple small blebs, it is possible that norepinephrine is inducing lytic cell death at higher doses. One of the achievements of this work is to decipher the correlation between  $\text{Ca}^{2+}$  sequestration in the subcellular domain and rupturing the membrane.<sup>33</sup> It has also been shown that norepinephrine with a lower dose may induce apoptosis when treated for a longer period of time.<sup>22</sup> The proposed study shows that a higher dose of norepinephrine can be specifically delivered to cancer cells to induce lytic cell death.<sup>42</sup>

Although HeLa cells are known to be a good model for testing the cytotoxicity of norepinephrine, the same study can also be performed in a heart cell model.<sup>43</sup> Based on these results, we plan to perform an *in vitro* preclinical study of H9c2 cells for toxicity analysis and estimation of the  $\text{Ca}^{2+}$  level in the presence of various levels of norepinephrine. Such a model may also provide a cell-based model for hypertrophy.<sup>23</sup> The other limitation of the proposed framework for dose–response analysis is that it gives only the complex waveform for  $\text{Ca}^{2+}$  oscillation but does not provide the actual  $\text{Ca}^{2+}$  concentration. To estimate the concentration of  $\text{Ca}^{2+}$  at the subcellular level, we need to

build a calibration curve by measuring Fluo-4 intensity under various concentrations of  $\text{Ca}^{2+}$  in a solution.<sup>5</sup>

For dimension reduction, in general, PCA, t-SNE, UMAP, and other mapping-based techniques can be implemented.<sup>33</sup> To address the inherent nonlinear nature, however, we implemented UMAP and t-SNE, and specifically chose UMAP since it takes less time. UMAP can save computation time significantly for high-content screening experiments.<sup>32</sup> In contrast, fuzzy clustering is a soft clustering in which the data point closer to the center of the cluster has a higher degree of membership compared to the one that is farthest. The major disadvantage of using FCM, however, is *a priori* specification of the number of clusters. Hence, further improvements can be proposed based on HDBSCAN (hierarchical density-based spatial clustering of applications with noise) clustering in the future, which can be used for automation in the selection of cluster numbers.<sup>44</sup> Furthermore, to achieve fully automated analysis, an image-processing module coupled with the proposed dimension reduction and clustering can be used as a high-throughput data analysis workflow toward toxicity mapping. Also, the proposed computational tool can be used for analysis of cytosolic  $\text{Ca}^{2+}$  measured through genetic sensors.<sup>12</sup>

The results show that higher concentration of norepinephrine induces sequestering of  $\text{Ca}^{2+}$  in subcellular parts during the dynamic cell death process. It is known that such an increase in cytosolic  $\text{Ca}^{2+}$  leads to an increase in mitochondrial membrane potential and thereby causes damage to epithelial cells.<sup>27</sup> Norepinephrine is known to induce IP3R1 [IP3 (inositol 1,4,5-trisphosphate) receptor subtype 1] activation, which leads to  $\text{Ca}^{2+}$  release from the endoplasmic reticulum (ER) to the cytosol.<sup>45–47</sup> Also, previous studies indicate that IP3R3 may have a significant role in controlling cell death in HeLa cells and other cells.<sup>48</sup> The proposed tool can be used to investigate the role of IP3R3 channels involved in the sequestration of  $\text{Ca}^{2+}$  in the mitochondria. In addition, mathematical modeling can be performed to find the roles of various subtypes of IP3 receptor in the regulation of  $\text{Ca}^{2+}$  sequestration. Further channel-blocking experiments can be performed to identify the role of IP3R3. Also, a quantitative analysis of mitochondrial  $\text{Ca}^{2+}$  (Rhod dye) and correlation with  $\text{Ca}^{2+}$  sequestration can be useful for understanding the progression of cell death dynamics.

## Acknowledgments

The authors thank Dr. Narasimhan Gautam for providing the research facilities at Washington University in St. Louis, and we also thank the valuable contributions of Vani Kalyanraman in setting the initial stages of the project on live cell imaging. We acknowledge Dr. Soumya Jana for his valuable contribution in framing the computational methods.

## Author Contributions

Manohar Kuruba, Suman Gare, and Lopamudra Giri: conceptualization and methodology development; Manohar Kuruba, Suman Gare, and Soumita Chel: data analysis; Suman Gare and Vaibhav Dhyani: visualization and analysis; and Manohar Kuruba, Lopamudra Giri, and Suman Gare: writing the original draft.


## Declaration of Conflicting Interests

The authors declared no potential conflicts of interest with respect to the research, authorship, and/or publication of this article.

## Funding

The authors disclosed receipt of the following financial support for the research, authorship, and/or publication of this article: This work was funded in part by BT/PR22239/NNT/28/1269/2017. This work was also funded by BT/PR21261/MED/31/348/2016. We also thank Department of Science and Technology for providing the Fellowship granted to Kuruba Manohar.

## ORCID iDs

Kuruba Manohar  <https://orcid.org/0000-0001-8902-206X>  
Lopamudra Giri  <https://orcid.org/0000-0002-2352-7919>

## References

- Hajnoczky, G.; Davies, E.; Madesh, M. Calcium Signaling and Apoptosis. *Biochem. Biophys. Res. Commun.* **2003**, *304*, 445–454.
- Dhyani, V.; Gare, S.; Gupta, R. K.; et al. GPCR Mediated Control of Calcium Dynamics: A Systems Perspective. *Cell. Signal.* **2020**, *74*, 109717.
- Jia, H.; Rochefort, N. L.; Chen, X.; et al. In Vivo Two-Photon Imaging of Sensory-Evoked Dendritic Calcium Signals in Cortical Neurons. *Nat. Protoc.* **2011**, *6*, 28–35.
- Prevedel, R.; Yoon, Y. G.; Hoffmann, M.; et al. Simultaneous Whole-Animal 3D Imaging of Neuronal Activity Using Light-Field Microscopy. *Nat. Methods* **2014**, *11*, 727–730.
- Zheng, K.; Jensen, T. P.; Rusakov, D. A. Monitoring Intracellular Nanomolar Calcium Using Fluorescence Lifetime Imaging. *Nat. Protoc.* **2018**, *13*, 581–597.
- Monteith, G. R.; Bird, G. S. Techniques: High-Throughput Measurement of Intracellular Ca(2+)—Back to Basics. *Trends Pharmacol. Sci.* **2005**, *26*, 218–223.
- St Croix, C. M.; Shand, S. H.; Watkins, S. C. Confocal Microscopy: Comparisons, Applications, and Problems. *BioTechniques* **2005**, *39*, S2–S5.
- Schober, L.; Büttner, E.; Laske, C.; et al. Cell Dispensing in Low-Volume Range with the Immediate Drop-on-Demand Technology (I-DOT). *J. Lab. Autom.* **2015**, *20*, 154–163.
- Wang, J.; Wu, M.-Y.; Tan, J.-Q.; et al. High Content Screening for Drug Discovery from Traditional Chinese Medicine. *Chinese Med.* **2019**, *14*, 5.
- Kriston-Vizi, J.; Flotow, H. Getting the Whole Picture: High Content Screening Using Three-Dimensional Cellular Model Systems and Whole Animal Assays. *Cytometry A* **2017**, *91*, 152–159.
- Martinez, N. J.; Titus, S. A.; Wagner, A. K.; et al. High-Throughput Fluorescence Imaging Approaches for Drug Discovery Using In Vitro and In Vivo Three-Dimensional Models. *Expert Opin. Drug Discov.* **2015**, *10*, 1347–1361.
- Wu, N.; Nishioka, W. K.; Derecki, N. C.; et al. High-Throughput-Compatible Assays Using a Genetically-Encoded Calcium Indicator. *Sci. Rep.* **2019**, *9*, 12692.
- Garner, K. L. High Content Imaging for Monitoring Signalling Dynamics in Single Cells. *J. Mol. Endocrinol.* **2020**, *65*, R91–R100.
- Leary, E.; Rhee, C.; Wilks, B. T.; et al. Quantitative Live-Cell Confocal Imaging of 3D Spheroids in a High-Throughput Format. *SLAS Technol.* **2018**, *23*, 231–242.
- Movsisyan, N.; Pardo, L. A. Measurement of Microtubule Dynamics by Spinning Disk Microscopy in Monopolar Mitotic Spindles. *J. Vis. Exp.* **2019**, 1–9.
- Mitchell, D. E.; Martineau, É.; Tazerart, S.; et al. Probing Single Synapses via the Photolytic Release of Neurotransmitters. *Front. Synaptic Neurosci.* **2019**, *11*, 1–14.
- Mella, R. M.; Kortazar, D.; Roura-Ferrer, M.; et al. Nomad Biosensors: A New Multiplexed Technology for the Screening of GPCR Ligands. *SLAS Technol.* **2018**, *23*, 207–216.
- Predescu, D. V.; Crețoiu, S. M.; Crețoiu, D.; et al. G Protein-Coupled Receptors (GPCRs)-Mediated Calcium Signaling in Ovarian Cancer: Focus on GPCRs Activated by Neurotransmitters and Inflammation-Associated Molecules. *Int. J. Mol. Sci.* **2019**, *20*.
- Gupta, R. K.; Swain, S.; Kankanamge, D.; et al. Comparison of Calcium Dynamics and Specific Features for G Protein-Coupled Receptor-Targeting Drugs Using Live Cell Imaging and Automated Analysis. *SLAS Discov.* **2017**, *22*, 848–858.
- Hasanin, A. M.; Amin, S. M.; Agiza, N. A.; et al. Norepinephrine Infusion for Preventing Postspinal Anesthesia Hypotension during Cesarean Delivery: A Randomized Dose-Finding Trial. *Anesthesiology* **2019**, *130*, 55–62.
- Park, S.; Lim, W.; You, S.; et al. Ochratoxin A Exerts Neurotoxicity in Human Astrocytes through Mitochondria-Dependent Apoptosis and Intracellular Calcium Overload. *Toxicol. Lett.* **2019**, *313*, 42–49.
- Fung, L.; Downey, K.; Ye, X. Y. Norepinephrine Intermittent Intravenous Boluses to Prevent Hypotension during Spinal Anesthesia for Cesarean Delivery: A Sequential Allocation Dose-Finding Study. *Anesth. Analg.* **2017**, *125*, 212–218.
- de Lima-Seolin, B. G.; Nemecek-Bakk, A.; Forsyth, H.; et al. Bucindolol Modulates Cardiac Remodeling by Attenuating Oxidative Stress in H9c2 Cardiac Cells Exposed to Norepinephrine. *Oxid. Med. Cell. Longev.* **2019**, *2019*, 6325424.
- Beurton, A.; Ducrocq, N.; Auchet, T.; et al. Beneficial Effects of Norepinephrine Alone on Cardiovascular Function and Tissue Oxygenation in a Pig Model of Cardiogenic Shock. *Shock* **2016**, *46*, 214–218.
- Levy, B.; Clere-Jehl, R.; Legras, A.; et al. Epinephrine versus Norepinephrine for Cardiogenic Shock after Acute Myocardial Infarction. *J. Am. Coll. Cardiol.* **2018**, *72*, 173–182.
- Sharkey, A. M.; Siddiqui, N.; Downey, K.; et al. Comparison of Intermittent Intravenous Boluses of Phenylephrine and Norepinephrine to Prevent and Treat Spinal-Induced Hypotension in Cesarean Deliveries: Randomized Controlled Trial. *Anesth. Analg.* **2019**, *129*, 1312–1318.
- Ishii, M.; Rohrer, B. Bystander Effects Elicited by Single-Cell Photo-Oxidative Blue-Light Stimulation in Retinal Pigment

- Epithelium Cell Networks. *Cell Death Discov.* **2017**, *3*, 16071.
28. Booiij, T. H.; Price, L. S.; Danen, E. H. J. 3D Cell-Based Assays for Drug Screens: Challenges in Imaging, Image Analysis, and High-Content Analysis. *SLAS Discov.* **2019**, *24*, 615–627.
  29. Feldt Muldoon, S.; Soltesz, I.; Cossart, R. Spatially Clustered Neuronal Assemblies Comprise the Microstructure of Synchrony in Chronically Epileptic Networks. *Proc. Natl. Acad. Sci. USA* **2013**, *110*, 3567–3572.
  30. Romano, S. A.; Pérez-Schuster, V.; Jouary, A.; et al. An Integrated Calcium Imaging Processing Toolbox for the Analysis of Neuronal Population Dynamics. *PLOS Comput. Biol.* **2017**, *13*, e1005526.
  31. Swain, S.; Gupta, R. K.; Ratnayake, K.; et al. Confocal Imaging and k-Means Clustering of GABA(B) and mGluR Mediated Modulation of Ca(2+) Spiking in Hippocampal Neurons. *ACS Chem. Neurosci.* **2018**, *9*, 3094–3107.
  32. Becht, E.; McInnes, L.; Healy, J.; et al. Dimensionality Reduction for Visualizing Single-Cell Data Using UMAP. *Nat. Biotechnol.* **2019**, *37*, 38–47.
  33. Vicar, T.; Raudenska, M.; Gumulec, J.; et al. The Quantitative-Phase Dynamics of Apoptosis and Lytic Cell Death. *Sci. Rep.* **2020**, *10*, 1566.
  34. Wang, Y.; Wang, H.; Ge, H.; et al. AG-1031 Induced Autophagic Cell Death and Apoptosis in C6 Glioma Cells Associated with Notch-1 Signaling Pathway. *J. Cell. Biochem.* **2018**, *119*, 5893–5903.
  35. Crowley, L. C.; Marfell, B. J.; Waterhouse, N. J. Analyzing Cell Death by Nuclear Staining with Hoechst 33342. *Cold Spring Harb. Protoc.* **2016**, 2016. doi:10.1101/pdb.prot087205.
  36. Venkateswarlu, K.; Suman, G.; Dhyani, V.; et al. Three-Dimensional Imaging and Quantification of Real-Time Cytosolic Calcium Oscillations in Microglial Cells Cultured on Electrospun Matrices Using Laser Scanning Confocal Microscopy. *Biotechnol. Bioeng.* **2020**, *117*, 3108–3123.
  37. Ali, M.; Jones, M. W.; Xie, X.; et al. TimeCluster: Dimension Reduction Applied to Temporal Data for Visual Analytics. *Vis. Comput.* **2019**, *35*, 1013–1026.
  38. Liao, M.; Liu, Y.; Yuan, J.; et al. Single-Cell Landscape of Bronchoalveolar Immune Cells in Patients with COVID-19. *Nat. Med.* **2020**, *26*, 842–844.
  39. Liang, S.; Han, D.; Yang, Y. Cluster Validity Index for Irregular Clustering Results. *Appl. Soft Comput.* **2020**, *95*, 106583.
  40. Ahmed, A. H. R.; Lee, J. H.; Gilchrist, M. L.; et al. Apoptosis Detection via Automated Algorithms to Analyze Biomarker Translocation in Reporter Cells. *Biotechnol. Bioeng.* **2020**, *117*, 1470–1482.
  41. Chernousova, S.; Epple, M. Live-Cell Imaging to Compare the Transfection and Gene Silencing Efficiency of Calcium Phosphate Nanoparticles and a Liposomal Transfection Agent. *Gene Ther.* **2017**, *24*, 282–289.
  42. Uchida, S.; Kobayashi, K.; Ohno, S.; et al. Induction of Non-Apoptotic Cell Death by Adrenergic Agonists in Human Oral Squamous Cell Carcinoma Cell Lines. *Anticancer Res.* **2019**, *39*, 3519–3529.
  43. Bloch, L.; Ndongson-Dongmo, B.; Kusch, A.; et al. Real-Time Monitoring of Hypertrophy in HL-1 Cardiomyocytes by Impedance Measurements Reveals Different Modes of Growth. *Cytotechnology* **2016**, *68*, 1897–1907.
  44. Chel, S.; Gare, S.; Giri, L. Detection of Specific Templates in Calcium Spiking in HeLa Cells Using Hierarchical DBSCAN: Clustering and Visualization of CellDrug Interaction at Multiple Doses\*. In Proceedings of the 2020 42nd Annual International Conference of the IEEE Engineering in Medicine & Biology Society (EMBC); IEEE: Piscataway (NJ), **2020**; pp 2425–2428.
  45. Bononi, A.; Giorgi, C.; Patergnani, S.; et al. BAP1 Regulates IP3R3-Mediated Ca<sup>2+</sup> Flux to Mitochondria Suppressing Cell Transformation. *Nature* **2017**, *546*, 549–553.
  46. Giri, L.; Patel, A. K.; Karunarathne, W. K. A.; et al. A G-Protein Subunit Translocation Embedded Network Motif Underlies GPCR Regulation of Calcium Oscillations. *Biophys. J.* **2014**, *107*, 242–254.
  47. Pinton, P.; Giorgi, C.; Siviero, R.; et al. Calcium and Apoptosis: ER-Mitochondria Ca<sup>2+</sup> Transfer in the Control of Apoptosis. *Oncogene* **2008**, *27*, 6407–6418.
  48. Marchi, S.; Marinello, M.; Bononi, A.; et al. Selective Modulation of Subtype III IP3R by Akt Regulates ER Ca<sup>2+</sup> Release and Apoptosis. *Cell Death Dis.* **2012**, *3*, 1–10.